Editors' Suggestion

Persistent Josephson tunneling between $Bi_2Sr_2CaCu_2O_{8+x}$ flakes twisted by 45° across the superconducting dome

Yuying Zhu,[1,2,*] Heng Wang,[3,*] Zechao Wang,[4,5,*] Shuxu Hu,[3] Genda Gu,[6] Jing Zhu,[4,5,†] Ding Zhang,[1,3,7,‡] and Qi-Kun Xue[1,3,8,§]

[1]*Beijing Academy of Quantum Information Sciences, Beijing 100193, China*
[2]*Hefei National laboratory, Hefei 230088, China*
[3]*State Key Laboratory of Low Dimensional Quantum Physics and Department of Physics, Tsinghua University, Beijing 100084, China*
[4]*National Center for Electron Microscopy in Beijing, School of Materials Science and Engineering, Key Laboratory of Advanced Materials (MOE), The State Key Laboratory of New Ceramics and Fine Processing, Tsinghua University, Beijing 100084, China*
[5]*Ji Hua Laboratory, Foshan, Guangdong 528200, China*
[6]*Condensed Matter Physics and Materials Science Department, Brookhaven National Laboratory, Upton, New York 11973, USA*
[7]*RIKEN Center for Emergent Matter Science (CEMS), Wako, Saitama 351-0198, Japan*
[8]*Southern University of Science and Technology, Shenzhen 518055, China*

(Received 29 October 2022; revised 15 October 2023; accepted 30 October 2023; published 16 November 2023)

There is a heated debate on the Josephson effect in twisted $Bi_2Sr_2CaCu_2O_{8+x}$ flakes. Latest results suggest the presence of either anomalously isotropic pairing or exotic $d + id$-wave pairing, in addition to the commonly believed d-wave one. Here, we address this controversy by fabricating ultraclean junctions with uncompromised crystalline quality at the junction interface. In the optimally doped regime, we obtain prominent Josephson coupling (2–4 mV) in multiple junctions with the twist angle of 45°, in sharp contrast to a recent report that shows two orders of magnitude suppression around 45° from the value at 0°. We further extend this study to the previously unexplored overdoped regime and observe pronounced Josephson tunneling at 45° together with Josephson diode effect up to 50 K. Our study helps establish the persistent presence of an isotropic pairing component across the entire superconducting phase diagram.

DOI: 10.1103/PhysRevB.108.174508

The pairing symmetry of cuprate superconductors is of vital importance for constructing a microscopic theory of high-temperature superconductivity [1–5]. Among proposals for phase-sensitive experiments to determine the pairing symmetry, one approach is to measure the Josephson coupling between two twisted cuprates along the c axis [Fig. 1(a)] [6–10]. Based on symmetry arguments, the Josephson tunneling between two d-wave superconductors vanishes when the twist angle along c axis is 45°, while it becomes the strongest when the twist angle is 0°. In the case of s-wave superconductors, the Josephson current persists to flow at 45°. Apart from the two scenarios, it was recently proposed [11–13] that cotunneling of Cooper pairs may occur between two cuprate monolayers at around 45°, giving rise to an emergent $d + id$ or $d + is$ wave pairing. Whether this exotic scenario is applicable to a strongly correlated system remains to be verified [14,15].

The intriguing proposals above call for careful experimental tests, which can be carried out by using $Bi_2Sr_2CaCu_2O_{8+x}$ (BSCCO). BSCCO naturally consists of a series of intrinsic Josephson junctions (IJJ) along the c axis [16,17] and it can be mechanically cleaved [18,19] into two parts and reassembled after twisting one of them with a predefined angle. This reassembling does not impose extra strain or induce changes in stoichiometry, allowing for the realization of atomically flat interface. By contrast, the in-plane Josephson junctions realized by epitaxy suffer from large structural distortion, tunneling plane misalignment and chemical inhomogeneity at grain boundaries [2,20,21]. Historically, the c-axis twisted BSCCO junctions were realized first by using bulk bicrystals [22] and whiskers [23,24]. These experiments favored isotropic pairing instead of d-wave pairing [6,8–10]. However, it remains unclear if these macroscopic junctions maintained atomically sharp and uniform interfaces [2]. There also existed technical issues such as overheating [22] and participation of multiple IJJ [23,24]. Recently, micrometer-sized BSCCO junctions were realized by the van der Waals (vdW) stacking technique. The atomically flat interface was revealed to extend over the complete junction area [4].

Despite this recent improvement, there is still a lack of consensus. Twisted junctions in the underdoped (UD) regime ($p < 0.1$) showed large Josephson coupling strength—the product of the Josephson critical current and normal state resistance (I_cR_n)—at 45° [4]. Yet another experiment [13] with samples in the nearly optimally doped (OP) regime reported suppression of I_cR_n by two orders of magnitude as the twist angle varied from 0° to 45°. The discrepancy requests further clarification. Notably, the twisted interfaces often exhibit

*These authors contributed equally to this work.
†jzhu@mail.tsinghua.edu.cn
‡dingzhang@mail.tsinghua.edu.cn
§qkxue@mail.tsinghua.edu.cn

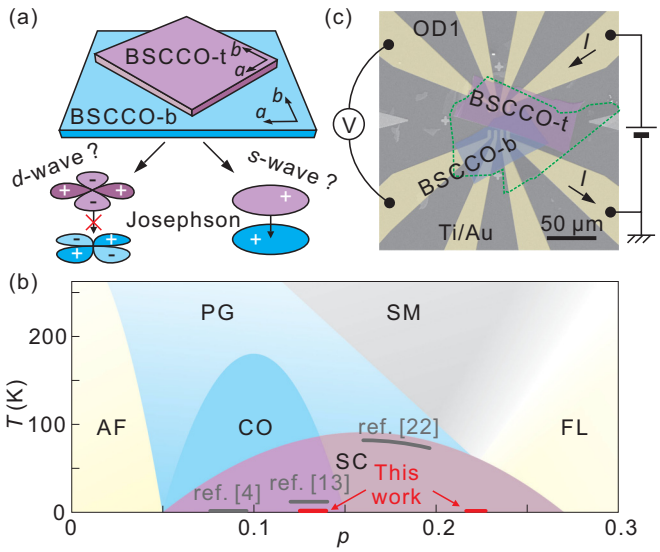

FIG. 1. (a) Schematic illustration of the twisted BSCCO junction and the theoretical expectation of Josephson tunneling based on different pairing symmetries. Here the top BSCCO (BSCCO-t) is rotated against the bottom BSCCO (BSCCO-b) by 45°. (b) Typical phase diagram of high-temperature cuprate superconductors including antiferromagnetism (AF), pseudogap (PG), charge ordering (CO), strange metal phase (SM), Fermi liquid (FL), and superconductivity (SC). Solid gray curves indicate the doping and temperature range of previous studies [4,13,22]. (c) False-colored SEM image of a twisted junction (sample OD1) with the electrical circuit for measuring the Josephson effect. For ac measurements, the dc voltage source and the voltmeter are replaced by the ac current source and the lock-in amplifier. BSCCO-t (BSCCO-b) is highlighted by a purple (blue) semitransparent shade while Ti/Au electrodes are highlighted by light-yellow semitransparent polygons. The green dashed polygon marks the hexagonal boron nitride (h-BN) protecting layer.

reduced signal and expanded interlayer spacing in atomically resolved images [4,13,25]. This extrinsic feature may hinder the observation of intrinsic effects. Moreover, the tunneling experiments so far focused on the doping regime from UD to OP [Fig. 1(b)], which is complicated by the charge ordering, pseudogap, and strange metal phases. By contrast, the OD regime is simpler and the corresponding cuprates exhibit well-established Fermi surfaces [26–28]. The twisted junction is even predicted to exhibit a nontrivial change of phase difference from OP to OD [15]. It is, therefore, highly favorable to extend the experimental study to the unexplored OD regime.

Here, we address the Josephson effect of twisted cuprate junctions in both OP and OD regimes [Fig. 1(b)]. By high-resolution transmission electron microscopy (HR-TEM), we demonstrate that our junctions meet the demanding requirement: All atoms at the interfaces possess the same signal intensities as those in the bulk, attesting to uncompromised crystalline quality. Transport experiments indicate (1) largely preserved doping level at the interface; (2) strong Josephson tunneling at twist angles close to 45°; (3) conventional temperature dependence of I_c, suggesting the absence of $d + id$-wave pairing. We further unveil asymmetric tunneling—Josephson diode effect—in some junctions. Finally, we compare I_cR_n at 45° and 0° in both OP and OD regimes. The weak angular dependence indicates a prominent isotropic pairing component over the whole phase diagram.

We fabricate the Josephson junctions [an example is given in Fig. 1(c)] out of high-quality single crystals of BSCCO [29] with a cold van der Waals stacking technique (Appendix A). The high-crystalline quality of the twisted junctions are demonstrated by TEM (Appendix B). Figures 2(a1)–2(a4) show representative images of four samples: OP1, OP2, OD1, and OD2. TEM also allows us to determine the exact twist angles by using the Kikuchi patterns [4]. The deviation from perfect 45° is as small as $0.05 - 0.1°$ for OP1 and OP2. We denote the twist angles as 44.9° (45.1° is equivalent). The cross-sectional images in Fig. 2 reveal the top and bottom BSCCO structures from different crystalline orientations. Furthermore, the bottom halves unveil, along two orthogonal directions ([010] for OP1 and OD1; [100] for OP2 and OD2), the uniaxial supermodulation that is innate of BSCCO. Notably, atoms of Bi, Sr, Cu, and Ca have comparable intensities at the interface and in the bulk. This is further supported by quantitative analyses in Appendix C. It suggests that the crystalline quality at the interface stays intact after the fabrication process—a clear improvement over previous experiments [4,13,25]. In addition, the thickness of the artificial junctions is slightly larger than that of IJJ: The distance between the two BiO planes at the twisted interface exceeds the bulk value by 12% [Fig. 7(c), see below]. We emphasize that TEM images of equivalently superb quality are obtained from multiple samples and in horizontally displaced regions across a few micrometers (see Figs. S1–S5 within the Supplemental Material, SM [30]).

With the well-characterized interfaces, we now analyze the transport results (these measurements were carried out before TEM). For the OP samples, temperature-dependent resistance shows a narrow superconducting transition with T_c close to that of the bulk Figs. 2(b1) and 2(b2) and Fig. S6 within the SM [30], confirming the preserved doping. For the OD samples [Figs. 2(b3) and 2(b4) and Fig. S7 within the SM [30]], however, the junction resistance reaches zero at around 50 K but the onset for the superconducting transition starts at a higher temperature of about 80 K. The higher onset temperature can be attributed to the top surface of the OD sample. There, oxygen loss occurs in the final fabrication step. Further support to this argument is given in Appendix D. Interestingly, OP junctions do not suffer from this problem, presumably because their oxygen content is more stable. We also remark that parallel conduction can plague the study of junctions fabricated at room temperature [4,25]: The interface can turn insulating but leave the rest of the flake superconductive.

Figures 2(c1)–2(c4) show tunneling characteristics. The single vertical branch at zero bias reflects the Josephson effect between the two twisted cuprate layers. The IJJ do not contribute here because their critical currents are much higher—due to the larger tunneling area and relatively thinner barrier—and are not reached in our measurement [31]. We obtain the normal state resistance R_n from the section with $I > I_c^+$ and $I < I_c^-$(dashed lines). Figure S9 (within the SM [30]) demonstrates that $1/R_n$ is proportional to the junction area. The extracted I_cR_n value reaches 3.5 mV in OP1. The critical voltage V_c, which also reflects the Josephson

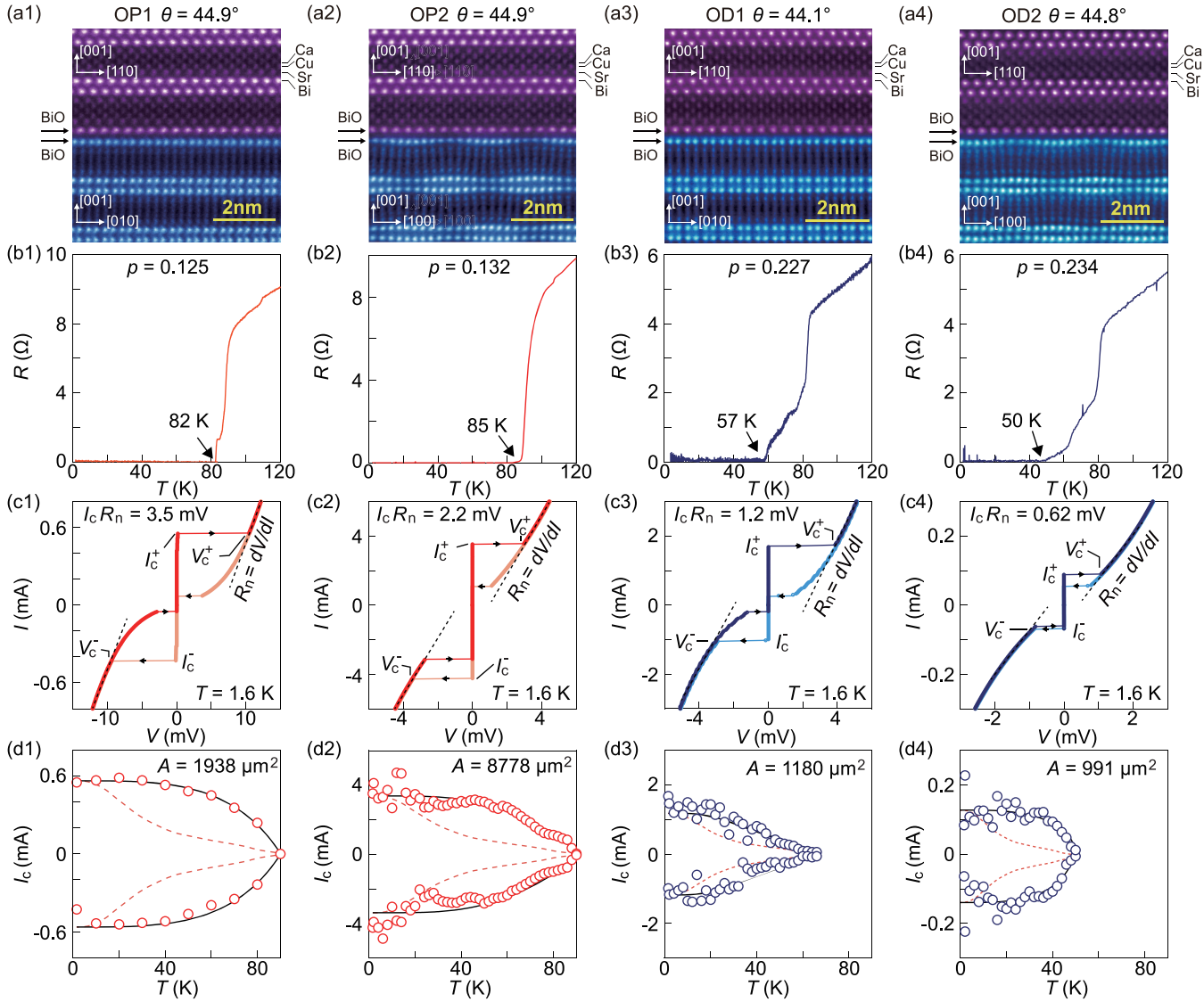

FIG. 2. [(a1)–(a4)] Cross-sectional high-angle annular dark-field scanning transmission electron microscopy (HAADF-STEM) images of four twisted BSCCO junctions (OP1, OP2, OD1, and OD2). Top and bottom BSCCO are highlighted by purple and blue shades. The unidirectional supermodulation runs along [100], giving rise to wavy undulation in the bottom section of OP2 and OD2. [(b1)–(b4)] Temperature-dependent resistance across the junctions. Arrows mark T_c. [(c1)–(c4)] Tunneling characteristics at $T = 1.6$ K. Darker (lighter) color reflects data points taken in the positive (negative) sweeping direction. Dashed lines indicate the extraction of R_n. The extracted I_cR_n values are indicated in the panels. $V_c^+(V_c^-)$ marks the critical voltage when the current is just above I_c^+ (below I_c^-). [(d1)–(d4)] Temperature dependence of the critical current. Junction areas are listed in the panels. Dashed curves are the theoretical prediction based on $d + id$ pairing [12]. Solid curves are guide to the eye.

coupling strength [13,25], is as high as 10 mV. The large I_cR_n here is in sharp contrast to the previous report in the same doping regime, which showed I_cR_n (44.9°) as small as 0.19 mV. The difference could arise from statistical fluctuation because only a few samples have been reported to be within $45.0 \pm 0.1°$ in OP (OP1 and OP2 in our case and one in Ref. [13]). We will also discuss the differences in the fabrication steps in the end.

Our results are inconsistent with the $d + id$ or $d + is$-wave pairing scenario [12]. Dashed curves in Figures 2(d1)–2(d4) indicate the predicted temperature dependence for this exotic pairing [12]. In contrast, our experimental results show quite standard behaviors with saturation of I_c at $T < 0.5T_c$. At twist angles notably away from 45°, a nonmonotonic temperature dependence was also predicted to be evidence for the exotic pairing [12]. In experiment, we indeed observe nonmonotonic or nonstandard temperature dependence (Fig. S8 within the SM [30]), but the nonmonotonic behavior even appears at 0° [Fig. S8(g)]. It indicates that the junctions may be influenced by some extrinsic factors, such as unintentional flux trapping. Similar suppression of I_c at low temperatures was observed in IJJ under a small magnetic field [32].

Interestingly, we find that trapped fluxes seem to cause asymmetric tunneling in some devices [33]. A typical example of such a Josephson diode effect (JDE) [34] is provided in Fig. 3. The Josephson critical current in the positive axis is obviously larger than the absolute value in the negative axis,

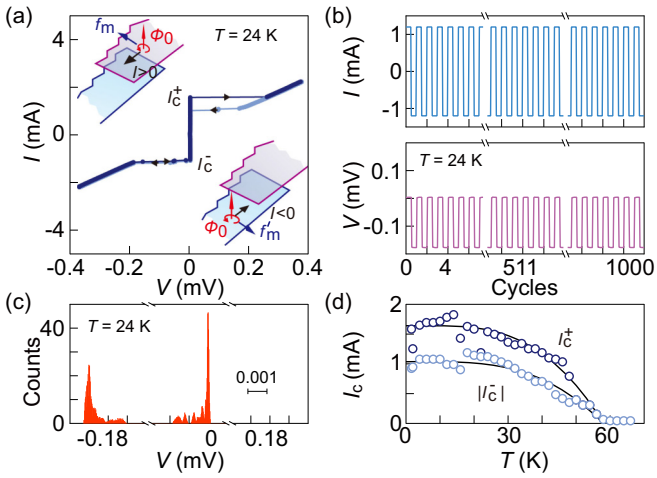

FIG. 3. (a) Current-voltage characteristics of an OD junction with a nominal twist angle of 45° at $T = 24$ K. Dark and light colors indicate data obtained in opposite sweeping directions, as indicated by the arrows. Data are obtained at nominally zero magnetic field. Insets schematically illustrate the magnus force (f_m/f'_m) experienced by a vortex under the positive/negative current. Contrast in the edge roughness could result in asymmetric flux flow when the current direction reverses. (b) Junction voltage (bottom) under the square wave of excitation current (±1.2 mA, 0.03 Hz) (top) at $T = 24$ K. (c) Histograms of the measured junction voltage data in (b). (d) Temperature-dependent critical currents in two directions. Solid curves are guide to the eye.

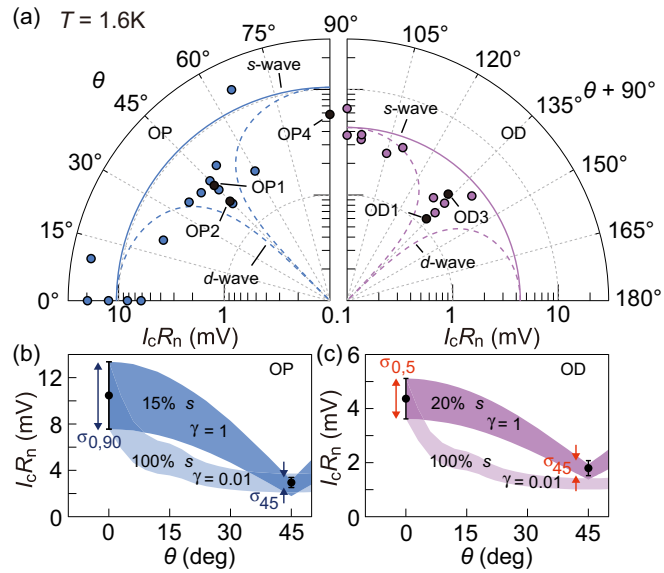

FIG. 4. (a) Fan-chart diagrams of I_cR_n as a function of twist angles. Filled symbols have angular values determined by TEM. Other data points have nominal twist angles. T_c for OP (OD) is in the range of 82 to 88 (57 to 67) K. [(b),(c)] Comparison between the averaged I_cR_n at $\theta(0°, 90°)/\theta(0°, 5°)$ and that at 45°. Error bars are from sampling standard deviations. Shaded bands with darker colors represent the theoretically expected behavior for a mixture of s wave and d wave. The tunneling is considered to be strongly incoherent as represented by $\gamma = 1$. The upper and lower bounds of the band take into account the data scattering $\sigma_{0,90}$ (at 0° and 90°) or $\sigma_{0,5}$ (at 0° and 5°). Shaded bands with lighter colors are theoretically calculated angular dependence for pure s wave with enhanced coherence in tunneling ($\gamma = 0.01$). Details of the calculation is given in Appendix E.

i.e., $I_c^+ > |I_c^-|$. The asymmetry factor $\eta = \frac{I_c^+ - |I_c^-|}{I_c^+ + |I_c^-|}$ is as high as 26% at 1.6 K. This asymmetry is quite stable such that the rectification effect over one thousand repetitions can be achieved [Figs. 3(b) and 3(c)]. It also persists over the entire superconducting regime exceeding 50 K [Fig. 3(d)]. In Fig. S10 within the SM [30], we demonstrate that a junction between BSCCO-2212 and $Bi_2Sr_{2-x}La_xCuO_{6+y}$ (BSCCO-2201) hosts vanishingly small η, despite obvious broken inversion symmetry at the interface. Symmetry breaking is therefore unlikely to account for JDE in Fig. 3. Although a 45°-twist junction is used in Fig. 3, similar behaviors are found at $\theta = 0°$ as well (Fig. S11 within the SM [30]). There, we obtain the peak-dip structure of η as a function of B with its center at 1 mT away from 0 T, clearly suggesting a remanent field. Such a small magnetic field may cause trapped fluxes in the junction. A rougher edge on one side of the sample [insets in Fig. 3(a)] may impede the transverse flow of these fluxes in one of the current directions, giving rise to a nonzero η [32,35]. Although this scenario remains highly speculative, our experiments suggest that future search for nonmonotonic $I_c(T)$ of intrinsic origins requires a carefully designed shield to avoid stray magnetic fields.

In Fig. 4(a), we provide an overview of I_cR_n [36] as a function of twist angles at both OP and OD. Similar plots but for V_c are given in Fig. S12 within the SM [30]. We observe appreciable I_cR_n and V_c in multiple samples around 45°. These data points apparently fall outside the expected behavior of a pure d-wave pairing symmetry. However, I_cR_n or V_c indeed shows a drop as θ increases from 0° to 45°, if comparing the maximal values obtained at different angles. This decrease can be further appreciated in Figs. 4(b) and 4(c), where averaged values of I_cR_n at 45 ± 1° for OP or 45 ± 2° for OD are compared with those around 0° and 90°. On the one hand, this angular dependence can be explained by a mixture of isotropic s-wave and anisotropic d-wave components [4]. The shaded stripes (darker colors) show the expected angular behavior for a mixture of 15%/20% s-wave and 85%/80% d-wave for OP/OD junctions. They yield values at 45° in agreement with experiment. It indicates a substantial isotropic pairing component (15–20%), comparable to that in $YBa_2Cu_3O_7$ (15%) [37]. On the other hand, the decreasing trend can be solely attributed to reduced overlap between two sets of bands in momentum space under c-axis rotation—an orbital effect [4,38]. We consider tunneling between two 100% s-wave superconductors with tunneling coherence that is 100 times higher than that in the s/d mixed situation [6]. The shaded bands with lighter colors in Figs. 4(b) and 4(c) show the calculated behaviors. They also reproduce the suppressed I_cR_n at 45° observed in experiment. In reality, the two scenarios may both participate in determining the angular dependence. The estimated portion of 15–20% of s wave only represents a lower bound.

Finally, we discuss differences between our fabrication process and that described in Ref. [13]. First, the sample cleavage and stacking were carried out at different temperatures: ⩽ –50 °C here and ⩽ –90 °C in Ref. [13]. We argue that this difference is unlikely to account for the large discrepancy

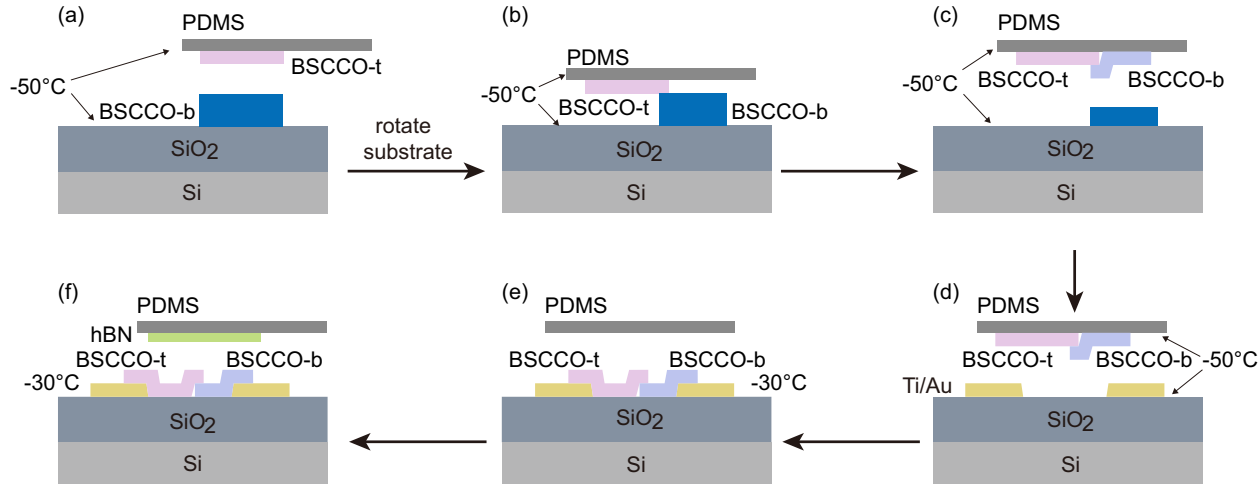

FIG. 5. Key sample fabrication steps carried out the in the Ar glovebox. The indicated temperatures were measured by two sensors attached to the substrate holder and the cantilever, respectively. (a) *In situ* sample cleavage into two flakes: BSCCO-t and BSCCO-b. (b) Junction formation by stacking BSCCO-t and BSCCO-b with a small overlap. Here BSCCO-b has been rotated against BSCCO-t along the c axis by a designated angle. (c) Pick-up of the twisted junction. A second cleavage can happen in BSCCO-b. (d) Relocation of the junction to another substrate with prepatterned electrodes. The pristine and prepatterned substrates are placed side by side on the same sample holder. (e) Release of the BSCCO stack. (f) Capping the junction with a h-BN flake.

in the tunneling results because (1) a higher temperature of $-40\,^{\circ}$C [19] was shown to be sufficient for protecting superconductivity even in few-layer BSCCO; (2) T_c in our junctions is nearly the same as in the bulk, attesting to preserved doping. Second, an additional step for metal deposition on top of the junction was used in Ref. [13], whereas we use only prepatterned electrodes. Our recipe guarantees that the sample always stays on the same cold stage throughout the whole fabrication process. Third, all our junctions are capped by hexagonal boron nitride for protection. This step turns out to be crucial even for thick samples [39]. The latter two technical modifications can better protect the junction and may help underpin intrinsic tunneling effects.

In summary, we fabricate twisted BSCCO junctions with unprecedentedly high crystalline quality at the interface. We observe strong Josephson tunneling and conventional temperature dependence at the twist angle very close to 45°. Intriguingly, some junctions show asymmetric critical currents in two current directions. From the angular dependence of the Josephson coupling, we conclude that there exists an indispensable isotropic pairing component in our twisted Josephson junctions.

ACKNOWLEDGMENTS

This work is financially supported by the Ministry of Science and Technology of China (Grants No. 2022YFA1403103, No. 2017YFA0302902); National Natural Science Foundation of China (Grants No. 12141402, No. 12004041, No. 12274249); Innovation Program for Quantum Science and Technology (Grant No. 2021ZD0302600). The work at BNL was supported by the US Department of Energy, office of Basic Energy Sciences, Contract No. DE-SC0012704.

APPENDIX A: METHOD

High quality crystals were grown by the traveling floating zone method with the details described in Ref. [29]. Crystals in the OP ($T_c = 87$ K) and OD ($T_c = 50 - 70$ K) regimes were employed. The whole fabrication process of junctions was carried out on a home-built transfer stage inside a glovebox filled with argon (H_2O < 0.01 ppm, O_2 < 0.01 ppm). The transfer stage allows multiaxis (x, y, z, and θ) motor-driven motion of the sample relative to a cantilever under a microscope.

Figure 5 shows the key steps for making the twisted junctions. We prepared polydimethylsiloxane (PDMS) by using Dow Corning Sylgard 184 (base: curing agent = 10:1) baked at 120°C on a sapphire plate. The PDMS on the sapphire plate was then loaded onto the cantilever, with the PDMS side facing downward. Two SiO_2/Si substrates were placed on the same sample stage: one bare substrate and one with prepatterned Ti/Au (5/40 nm) electrodes realized by standard photolithography and e-beam evaporation.

We first deposited BSCCO flakes onto the bare substrate via the standard mechanical exfoliation. Both the cantilever and the sample stage were then cooled to $-50\,^{\circ}$C (as measured by the PT-100 sensors), by copper cold fingers connected to a home-built liquid nitrogen dewar inside the glovebox. We used the PDMS to cleave a selected flake *in situ* into two pieces [Fig. 5(a)]. Afterwards, the substrate was rotated to the designated angle. We moved the sample stage relative to the cantilever such that the two cleaved flakes can have a small overlapping area [Fig. 5(b)]. The sample stage was further raised to bring the PDMS into contact with the top surfaces of both top and bottom BSCCO. Subsequently, we separated the cantilever from the sample stage. A stack consisting of both the top Bi-2212 and the bottom Bi-2212 could be picked up this way. It was often accompanied by

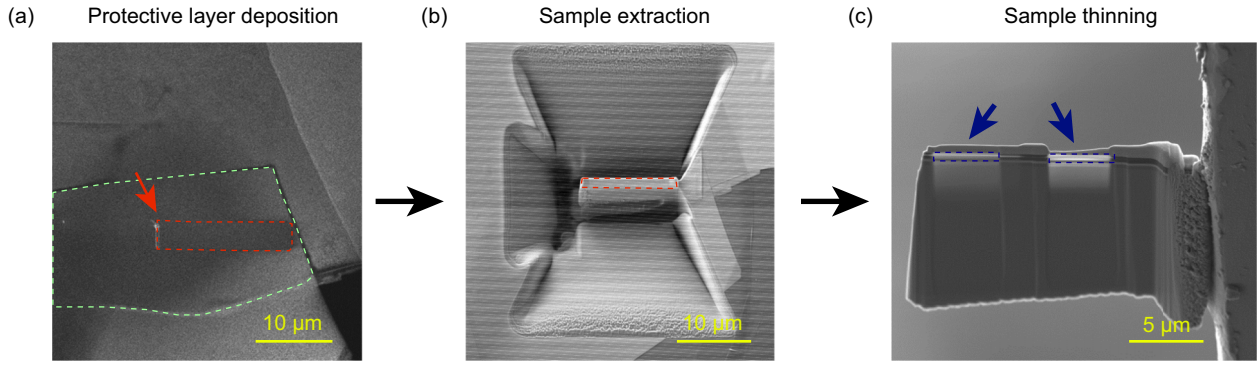

FIG. 6. Fabrication steps for TEM. (a) Deposition of a protective layer (Pt) with a working area of 5 μm × 16 μm on the junction region. Green and red dashed lines demarcate the junction region and the working area for TEM studying. (b) Cutting and extraction of a slab in the junction area. (c) Thinning of two regions (marked by blue dashed rectangles) for TEM imaging. The lateral size is approximately 5 μm. A series of TEM images are collected from these two regions.

another cleavage in the bottom Bi-2212 flake, as indicated in Fig. 5(c).

We then transferred the junction to the prepatterned substrate [Fig. 5(d)]. Here, we released the junction onto the substrate as the sample stage was at about −30° by detaching it from the cold finger [Fig. 5(e)]. The top and the bottom BSCCO flakes (about 30–200-nm thick) were contacted from the bottom by the electrodes. In order to protect the central area from direct exposure to air, we capped it with a flake of hexagonal boron nitride (h-BN) [Fig. 5(f)].

After the stacking in the glovebox, samples were wired to chip carriers (each within an hour at ambient conditions) and loaded into the closed-cycle helium-free cryogenic systems for measurements. We measured resistance by using the standard lock-in technique with a typical excitation current of 1 μA at 13.3 Hz. The tunneling characteristics was carried out in a four-terminal configuration by using a dc current source and a dc nanovoltmeter. TEM studies were carried out after the transport characterizations.

APPENDIX B: TEM CHARACTERIZATION

1. FIB sample preparation

Samples for cross-sectional transmission electron microscopy (TEM) were prepared by FIB with a Ga ion beam (30 kV) using the Zeiss Auriga workstation. Figure 6 illustrates the key fabrication steps. We selected a rectangular region of the junction area to deposit Pt as the protective layer. A vertical slab with a horizontal length of about 16 μm was cut out by the Ga ion beam at 30 kV. Subsequently, the two sides exposing the cross-section of the BSCCO stack were lightly polished several times by low energy Ar ion milling (ramping down from 900 eV to 500 eV). This milling helped remove the amorphous layers on the surface, which were caused by the Ga ion beam. It also resulted in uniformly large and thin areas that were suitable for TEM imaging [Fig. 6(c)].

2. High-angle annular dark-field (HADDF) method

HAADF-STEM experiments were carried on FEI-Titan Cubed Themis 60-300. It can collect high-resolution STEM images with a spatial resolution of 0.06 nm. The microscope possesses a high brightness electron gun (X-FEG with a monochromator), a probe corrector, an image corrector, and a postcolumn imaging energy filter (Gatan Quantum 965 Spectrometer). The semiconvergence angle of the electron beam and the collection angle of the HAADF detector are 25 mrad and 64–200 mrad, respectively. Before the data acquisition, samples were placed in the interested region for stabilizing a few hours. To further reduce any remaining thermal drift, a fast scanning speed (0.4 pixel/μs) was used for collecting each image with 1024 × 1024 pixels.

APPENDIX C: QUANTITATIVE ANALYSIS OF THE INTERFACIAL CRYSTALLINE STRUCTURE

Here we demonstrate the high crystalline quality achieved at our Josephson junction by quantitatively analyzing the TEM images. For the superconducting layer, we take a horizontal line cut along the CuO_2 plane of the top BSCCO next to the twist boundary. We compare this line profile with that obtained from the CuO_2 plane far away from the interface, as shown in Fig. 7(a). Each peak represents one row of Cu atoms. Clearly, the two line profiles are closely matched. Figure 7(b) shows the averaged intensity profile along the c axis. It demonstrates that the double BiO planes at the twist boundary (indicated by red arrows) exhibit intensity peaks comparable to those from the bulk (indicated by black arrows). In general, the artificial interface is atomically flat without any reconstruction or wrinkles. In addition, we point out that the thickness of the artificial junctions is slightly larger than that of IJJ. The separation between the vertical dashed lines in Fig. 7(b) represent the distance between nearest-neighbored BiO layers in the bulk. We observe that the actual peaks from the BiO plane at the twist boundary (red arrows) situate away from the dashed lines. Figures 7(c) and 7(d) summarize the distances between the two BiO planes ($d_{\mathrm{Bi-Bi}}$) and the two Ca planes ($d_{\mathrm{Ca-Ca}}$) across the interface. On average, $d_{\mathrm{Bi-Bi}}$ is larger than the bulk value by 12%. Consequently, $d_{\mathrm{Ca-Ca}}$ across the artificial interface is 2.4% larger than that of the bulk.

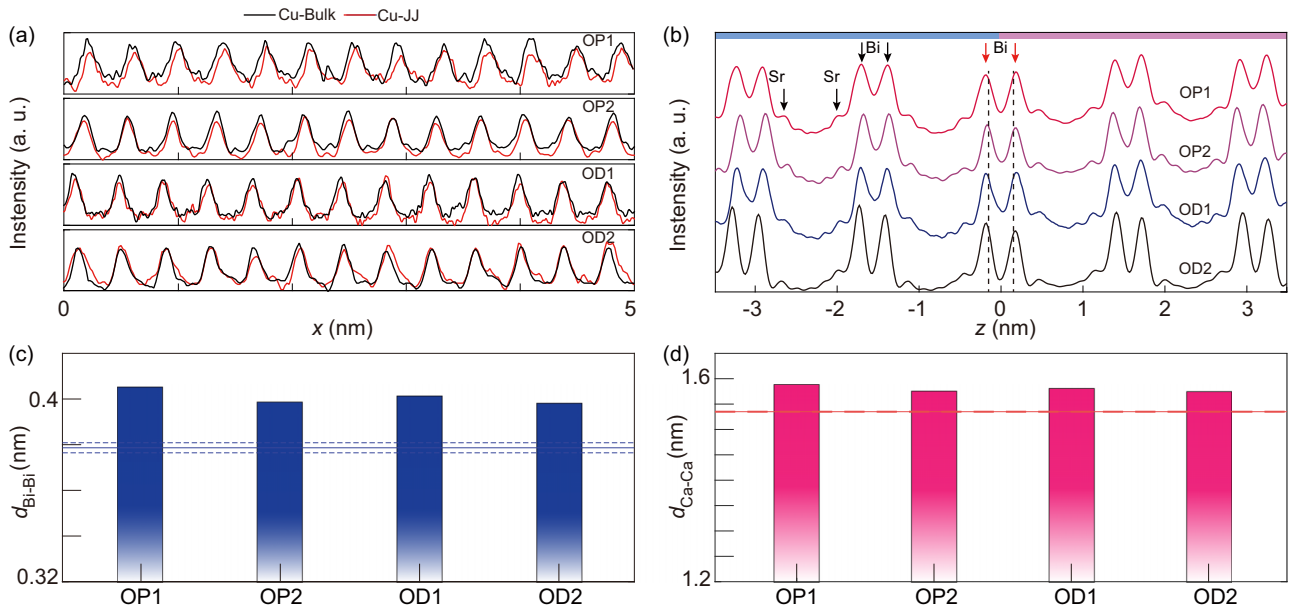

FIG. 7. (a) Intensity profile of the CuO_2 plane close to the interface (red) and that in the bulk (black) for sample OP1, OP2, OD1, and OD2. (b) Normalized intensity profiles along the c axis. Red arrows mark the peaks from BiO layers at the interface. Here, $z = 0$ marks the twist boundary. Curves are horizontally offset for clarity. Purple and blue bands on the top indicate the top and bottom BSCCO. [(c),(d)] Extracted interlayer distances d_{Bi-Bi} and d_{Ca-Ca} in our four twisted samples. Here, d_{Bi-Bi} (d_{Ca-Ca}) is the distance between the two nearest-neighbored BiO (Ca) planes at the twisted interface. The solid lines represent the mean value in the intrinsic junction. The dashed lines indicate the error bar, as defined by the standard deviation.

APPENDIX D: PRESERVATION OF DOPING LEVEL AT THE INTERFACE IN OD JUNCTIONS

For OD junctions, the superconducting transition starts at about 80 K. This onset temperature T_{onset} is much higher than the temperature (about 50 K) at which the resistance drops to zero T_{c0}. There are also steps in the superconducting transition, indicating phase separations. Examples are shown in Fig. 2 and Fig. S7 within the SM [30]. These features reflect doping inhomogeneity in the sample. Here we demonstrate that this inhomogeneity stems from the loss of oxygen on the upper surface of the OD-BSCCO. The twisted interface, which is buried inside the BSCCO stack, largely retains the initial doping level.

Previous experiments on exfoliated BSCCO establish that oxygen out-diffusion is the predominant cause of doping variation in ultrathin flakes [18,19]. It is noteworthy that for a multilayer BSCCO flake, the oxygen out-diffusion happens in the outer layers while the doping level in the inner layers can be kept unaffected. This can explain why some BSCCO/BSCCO junction shows no Josephson tunneling across the twisted interface but the individual flakes display superconducting transition similar to the bulk [25]. During our sample fabrication process in Fig. 5, oxygen out-diffusion could happen in either the top or the bottom surfaces once they are exposed to the Ar atmosphere. Specifically, we list the possible oxygen-releasing surfaces of each step: (1) the bottom surface of BSCCO-t and the top surface of BSCCO-b in the first step after cleavage [Figs. 5(a) and 5(b)]; (2) the bottom surfaces of BSCCO-t and BSCCO-b during the third and fourth steps [Figs. 5(c) and 5(d)]; (3) the top surfaces of BSCCO-t and BSCCO-b in the fifth step [Fig. 5(e)].

To check if oxygen out-diffusion really occurs in the above-mentioned steps, we measure BSCCO-t and BSCCO-b separately [Figs. 8(a) and 8(b)] in two samples. Here, large h-BN flakes are selected to cover the complete BSCCO stacks, minimizing oxygen out-diffusion and surface degradation when the samples are out of the glovebox. Figures 8(c)–8(e) show that R_t and R_b from the individual flakes possess the same T_{c0} of 55–60 K. It indicates that oxygen loss at the bottom surfaces of both BSCCO-t and BSCCO-b is strongly suppressed. Otherwise, the doping level of the bottom surfaces would move from OD to OP. In the situation of parallel conduction channels contacted from the bottom [schematically drawn as inset to Figs. 8(d) and 8(e)], a bottom surface at OP would give rise to the appearance of zero resistance at around 80 K instead, in direct contrast to the experimental observation. We note that the situation is different if the top surfaces move to a lower doping because they cannot short-circuit the entire BSCCO stack in the bottom contacting configuration.

The bottom surfaces are exposed to the Ar atmosphere during the first to fourth steps. Their absence of oxygen loss clearly demonstrates that $-50\,^{\circ}$C is sufficient to quench the oxygen out-diffusion. Since the junction is formed at the same cryogenic temperature [Fig. 5(b)], its doping level must be preserved too. Still, we observe T_{onset} of about 80 K in both $R_{t/b}$ and R_j. As we have excluded oxygen out-diffusion in the first to fourth steps, we therefore conclude that oxygen out-diffusion only happens in the fifth step [Fig. 5(e)]. In other words, top surfaces of BSCCO-t and BSCCO-b lose oxygen at the slightly elevated temperature of $-30\,^{\circ}$C. We

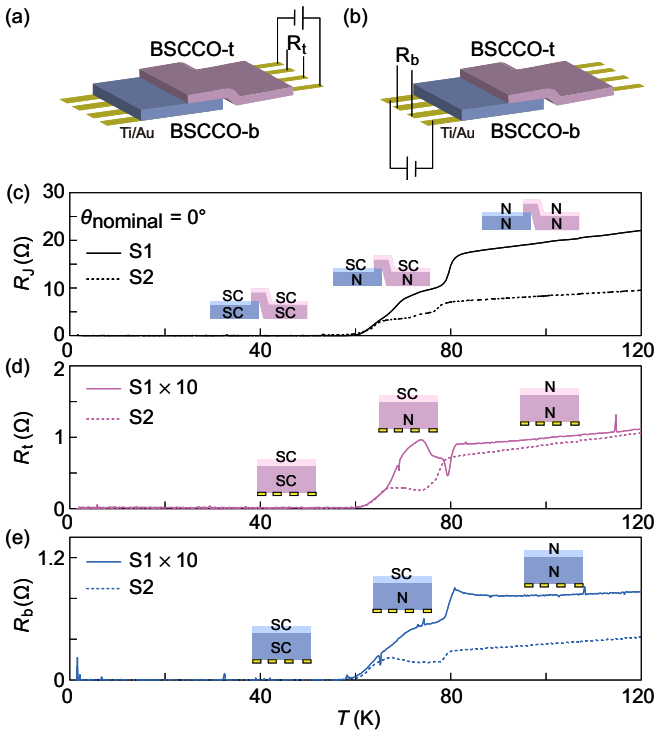

FIG. 8. [(a),(b)] Schematic drawings for measuring the resistances of the top and bottom layers separately. Here the complete BSCCO-t/BSCCO-b stack is covered by a h-BN flake (not shown). [(c)–(e)] Temperature-dependent resistances of the two samples (S1 and S2) taken either across the junction (c) or on the individual sides [(d),(e)]. The insets illustrate the parallel conduction. At temperatures above 80 K, the entire stack is in the normal state (N). Between 60 to 80 K, the top surfaces become superconducting (SC). Below 60 K, the entire stack becomes superconducting.

emphasize that this out-diffusion only affects the superoxygenated samples in the overdoped regime. The OP junctions do not show this behavior.

APPENDIX E: THEORETICAL CALCULATIONS

We use the formula as described in our previous paper (see Supplemental Material of Ref. [4]) to calculate the Josephson critical current at different twist angles. Here we mainly emphasize the modifications in notations. We use the following formula for the modulus square of the tunneling matrix element:

$$F(\boldsymbol{k},\boldsymbol{k}') = F_0 \exp\left(-\frac{|\boldsymbol{k}-\boldsymbol{k}'|^2 a^2}{2\pi^2\gamma^2}\right) \tag{E1}$$

where $\boldsymbol{k}$, $\boldsymbol{k}'$ are the momentum vector in the top and bottom layers, a is the lattice constant, and γ determines the degree of tunneling coherence. The tunneling is fully incoherent as $\gamma \to \infty$. We use the following gap function for the mixture of s-wave and d-wave pairing:

$$\Delta_{s+d} = (1-p)\cdot\Delta_0[cos(k_x a) - cos(k_y a)] + p\cdot\Delta_0. \tag{E2}$$

Here p represents the percentage of the isotropic s-wave component.

For numerical calculations, we set the temperature to 1.6 K and summed up 600 Matsubara frequencies to ensure convergence. The integrations were calculated by dividing each Brillouin zone of the two layers into a 100 by 100 lattice for the calculation with $\gamma = 1$ and 400 by 400 lattice for $\gamma = 0.01$.

[1] B. Keimer, S. A. Kivelson, M. R. Norman, S. Uchida, and J. Zaanen, From quantum matter to high-temperature superconductivity in copper oxides, Nature (London) **518**, 179 (2015).

[2] C. C. Tsuei and J. R. Kirtley, Pairing symmetry in cuprate superconductors, Rev. Mod. Phys. **72**, 969 (2000).

[3] Y. Zhong, Y. Wang, S. Han, Y.-F. Lv, W.-L. Wang, D. Zhang, H. Ding, Y.-M. Zhang, L. Wang, K. He *et al.*, Nodeless pairing in superconducting copper-oxide monolayer films on $Bi_2Sr_2CaCu_2O_{8+\delta}$, Sci. Bull. **61**, 1239 (2016).

[4] Y. Zhu, M. Liao, Q. Zhang, H.-Y. Xie, F. Meng, Y. Liu, Z. Bai, S. Ji, J. Zhang, K. Jiang, R. Zhong, J. Schneeloch, G. Gu, L. Gu, X. Ma, D. Zhang, and Q.-K. Xue, Presence of s-wave pairing in Josephson junctions made of twisted ultrathin $Bi_2Sr_2CaCu_2O_{8+\delta}$ flakes, Phys. Rev. X **11**, 031011 (2021).

[5] J.-Q. Fan, X.-Q. Yu, F.-J. Cheng, H. Wang, R. Wang, X. Ma, X.-P. Hu, D. Zhang, X.-C. Ma, Q.-K. Xue, and C.-L. Song, Direct observation of nodeless superconductivity and phonon modes in electron-doped copper oxide $Sr_{1-x}Nd_xCuO_2$, Nat. Sci. Rev. **9**, nwab225 (2022).

[6] R. A. Klemm, The phase-sensitive c-axis twist experiments on $Bi_2Sr_2CaCu_2O_{8+\delta}$ and their implications, Philos. Mag. **85**, 801 (2005).

[7] T. Yokoyama, S. Kawabata, T. Kato, and Y. Tanaka, Theory of macroscopic quantum tunneling in high-T_c c-axis Josephson junctions, Phys. Rev. B **76**, 134501 (2007).

[8] G. B. Arnold and R. A. Klemm, Theory of coherent c-axis Josephson tunneling between layered superconductors, Phys. Rev. B **62**, 661 (2000).

[9] A. Bille, R. A. Klemm, and K. Scharnberg, Models of c-axis twist Josephson tunneling, Phys. Rev. B **64**, 174507 (2001).

[10] R. A. Klemm, Theory of $Bi_2Sr_2CaCu_2O_{8+\delta}$ cross-whisker Josephson junctions, Phys. Rev. B **67**, 174509 (2003).

[11] O. Can, T. Tummuru, and R. Day, High-temperature topological superconductivity in twisted double-layer copper oxides, Nat. Phys. **17**, 519 (2021).

[12] T. Tummuru, S. Plugge, and M. Franz, Josephson effects in twisted cuprate bilayers, Phys. Rev. B **105**, 064501 (2022).

[13] S. Y. F. Zhao, N. Poccia, X. Cui, P. A. Volkov, H. Yoo, R. Engelke, Y. Ronen, R. Zhong, G. Gu, S. Plugge *et al.*, Emergent interfacial superconductivity between twisted cuprate superconductors, arXiv:2108.13455.

[14] X.-Y. Song, Y.-H. Zhang, and A. Vishwanath, Doping a moiré Mott insulator: A $t-J$ model study of twisted cuprates, Phys. Rev. B **105**, L201102 (2022).

[15] X. Lu and D. Sénéchal, Doping phase diagram of a Hubbard model for twisted bilayer cuprates, Phys. Rev. B **105**, 245127 (2022).

[16] R. Kleiner, F. Steinmeyer, G. Kunkel, and P. Müller, Intrinsic Josephson effects in $Bi_2Sr_2CaCu_2O_8$ single crystals, Phys. Rev. Lett. **68**, 2394 (1992).

[17] R. Kleiner and P. Müller, Intrinsic Josephson effects in high-T_c superconductors, Phys. Rev. B **49**, 1327 (1994).

[18] M. Liao, Y. Zhu, J. Zhang, R. Zhong, J. Schneeloch, G. Gu, K. Jiang, D. Zhang, X. Ma, and Q.-K. Xue, Superconductor-insulator transitions in exfoliated $Bi_2Sr_2CaCu_2O_{8+\delta}$ flakes, Nano Lett. **18**, 5660 (2018).

[19] Y. Yu, L. Ma, P. Cai, R. Zhong, C. Ye, J. Shen, G. D. Gu, X. H. Chen, and Y. Zhang, High-temperature superconductivity in monolayer $Bi_2Sr_2CaCu_2O_{8+\delta}$, Nature (London) **575**, 156 (2019).

[20] X. F. Zhang, D. J. Miller, and J. Talvacchio, Control of meandering grain boundary configurations in $YBa_2Cu_3O_y$ bicrystal thin films based on deposition rate, J. Mater. Res. **11**, 2440 (1996).

[21] Q. Jin and S. W. Chan, Grain boundary faceting in $YBa_2Cu_3O_{7-x}$ bicrystal thin films on $SrTiO_3$ substrates, J. Mater. Res. **17**, 323 (2002).

[22] Q. Li, Y. N. Tsay, M. Suenaga, R. A. Klemm, G. D. Gu, and N. Koshizuka, $Bi_2Sr_2CaCu_2O_{8+\delta}$ bicrystal c-axis twist Josephson junctions: A new phase-sensitive test of order parameter symmetry, Phys. Rev. Lett. **83**, 4160 (1999).

[23] Y. Takano, T. Hatano, A. Fukuyo, A. Ishii, M. Ohmori, S. Arisawa, K. Togano, and M. Tachiki, d-like symmetry of the order parameter and intrinsic Josephson effects in $Bi_2Sr_2CaCu_2O_{8+\delta}$ cross-whisker junctions, Phys. Rev. B **65**, 140513 (2002).

[24] Y. I. Latyshev, A. P. Orlov, A. M. Nikitina, P. Monceau, and R. A. Klemm, c-axis transport in naturally grown $Bi_2Sr_2CaCu_2O_{8+\delta}$ cross-whisker junctions, Phys. Rev. B **70**, 094517 (2004).

[25] J. Lee, W. Lee, G.-Y. Kim, Y.-B. Choi, J. Park, S. Jang, G. Gu, S.-Y. Choi, G. Y. Cho, G.-H. Lee, and H.-J. Lee, Twisted van der Waals Josephson junction based on a high-T_c superconductor, Nano Lett. **21**, 10469 (2021).

[26] B. Vignolle, A. Carrington, R. A. Cooper, M. M. J. French, A. P. Mackenzie, C. Jaudet, D. Vignolles, C. Proust, and N. E. Hussey, Quantum oscillations in an overdoped high-T_c superconductor, Nature (London) **455**, 952 (2008).

[27] Y. He, S.-D. Chen, Z.-X. Li, D. Zhao, D. Song, Y. Yoshida, H. Eisaki, T. Wu, X.-H. Chen, D.-H. Lu, C. Meingast, T. P. Devereaux, R. J. Birgeneau, M. Hashimoto, D.-H. Lee, and Z.-X. Shen, Superconducting fluctuations in overdoped $Bi_2Sr_2CaCu_2O_{8+\delta}$, Phys. Rev. X **11**, 031068 (2021).

[28] A. Zhao, Q. Gu, and R. A. Klemm, Angular dependence of the upper critical induction of clean s and $d_{x^2-y^2}$-wave superconductors with self-consistent ellipsoidal effective mass and Zeeman anisotropies, J. Phys.: Condens. Matter **34**, 355601 (2022).

[29] G. Gu, K. Takamuku, N. Koshizuka, and S. Tanaka, Large single crystal Bi-2212 along the c-axis prepared by floating zone method, J. Cryst. Growth **130**, 325 (1993).

[30] See Supplemental Material at http://link.aps.org/supplemental/10.1103/PhysRevB.108.174508 for (1) TEM images of five samples both in large and small scales. (2) Extended transport data set. (3) Transport and tunneling characteristics of a BSCCO-2201/BSCCO-2212 junction. (4) Josephson diode effect in a second sample..

[31] Extended Data Fig. 3 of: S. Ghosh, V. Patil, A. Basu, Kuldeep, D. A. Jangade, R. Kulkarni, A. Thamizhavel, and M. M. Deshmukh, High-temperature superconducting diode. arXiv:2210.11256.

[32] A. Yurgens, D. Winkler, T. Claeson, G. Yang, I. F. G. Parker, and C. E. Gough, $Bi_2Sr_2CaCu_2O_{8+\delta}$ intrinsic Josephson junctions in a magnetic field, Phys. Rev. B **59**, 7196 (1999).

[33] We became aware of a recent preprint reporting similar superconducting diode effect but in the OP regime instead of OD or UD regimes studied here: S. Ghosh, V. Patil, A. Basu, Kuldeep, D. A. Jangade, R. Kulkarni, A. Thamizhavel, M. M. Deshmukh, High-temperature superconducting diode. arXiv:2210.11256.

[34] H. Wu, Y. Wang, Y. Xu, P. K. Sivakumar, C. Pasco, U. Filippozzi, S. S. Parkin, Y. J. Zeng, T. McQueen, and M. N. Ali, The field-free Josephson diode in a van der Waals heterostructure, Nature (London) **604**, 653 (2022).

[35] D. Y. Vodolazov and F. M. Peeters, Superconducting rectifier based on the asymmetric surface barrier effect, Phys. Rev. B **72**, 172508 (2005).

[36] Samples with non-monotonic $I_c(T)$ are excluded because their Josephson coupling strengths may be underestimated.

[37] H. J. H. Smilde, A. A. Golubov, Ariando, G. Rijnders, J. M. Dekkers, S. Harkema, D. H. A. Blank, H. Rogalla, and H. Hilgenkamp, Admixtures to d-wave gap symmetry in untwinned $YBa_2Cu_3O_7$ superconducting films measured by angle-resolved electron tunneling, Phys. Rev. Lett. **95**, 257001 (2005).

[38] L. S. Farrar, A. Nevill, Z. J. Lim, G. Balakrishnan, S. Dale, and S. J. Bending, Superconducting quantum interference in twisted van der Waals heterostructures, Nano Lett. **21**, 6725 (2021).

[39] Y. Lee, M. Martini, T. Confalone, S. Shokri, C. N. Saggau, G. Gu, K. Watanabe, T. Taniguchi, D. Montemurro, V. M. Vinokur *et al.*, Encapsulating high-temperature superconducting twisted van der Waals heterostructures blocks detrimental effects of disorder, Adv. Mater. **35**, 2209135 (2023).